Integration and operation of a sUAS-based multi-modal imaging payload equipped with a novel communication system enabling autonomous platform control

Andrew M. Duncan[a], Bogdan Vacaliuc[a], Matthew D. Larson[a], Christopher Davis[a], David Hughes[a], and Katie Corcoran[a]

[a]Oak Ridge National Laboratory, Knoxville, USA

ABSTRACT

Oak Ridge National Laboratory presents a new UAS-mounted multi-modal imaging payload containing five sensors. We have integrated several distinct commercially available sensors onto a large Class-1 autonomous quadcopter aircraft: a LIDAR (Light Detection and Ranging) scanner, a hyperspectral pushbroom sensor, a multispectral camera, a longwave infrared thermal camera, and an RGB camera. The system integrates our proprietary Multi-modal Autonomous Vehicle Network (MAVNet) and communication system, allowing autonomous control via multiple communication networks. Using one common Global Navigation Satellite System (GNSS) and inertial navigation system (INS/GPS), imagery from all sensors are accurately and precisely geolocated and co-registered.

Keywords: sUAS, sensors, autonomous, communication system, remote sensing, sensor fusion

1. INTRODUCTION

Multispectral, hyperspectral, thermal, and light detection and ranging (LIDAR) are several of the most common modalities used in the remote sensing community. Multispectral and hyperspectral sensors provide spectral information that can be used to understand natural and artificial phenomena observable at the Earth's surface. Examples include mapping vegetation cover[1,2] and minerals,[3,4] monitoring urban growth[5] and damage assessment,[6] as well as monitoring water quality[7,8] and agricultural crop yield.[9,10] Thermal sensors provide data needed to study temperature and temperature changes,[11] which are used to monitor volcanic activity,[12] evapotranspiration of crops,[13] and ground water discharge.[14,15] LIDAR provides detailed information about the 3D structure of virtually any accessible natural or anthropogenic feature including forest structure[16] and mapping power lines.[17]

Multi-modal data collection allows for an improved understanding of Earths surface, as each modality offers unique properties that complement that of another modality. Examples of multi-modal remote sensing data collection, i.e., data fusion, include combining hyperspectral and LiDAR data to provide biomass spectra and 3D structure, respectively.[18–20] Spectra are often used to assess plant health, and LIDAR can accurately survey the morphological traits (e.g., height, volume) of an individual plant or an entire crop of plants.[16] It is often the case that multi-modal data fusion relies upon data collected from different platforms (e.g., satellite and airborne)[18,21,22] and acquisition times are often not coincident.[21,23] Different remote sensing platforms, acquisition times, and observational scales can introduce multi-dimensional and multi-temporal data artifacts, thus compounding the challenges of pre-processing data.[24]

Availability of accurately co-registered data is critical to successful data fusion. Accurately co-registered data of similar spatial resolution for different sensor types is limited when sensors are deployed on different platforms, acquired on different dates, or collected under different collection parameters (e.g., viewing geometry, solar geometry, atmospheric conditions). In recent years, the integration of multiple sensing modalities on one platform has become more common. Multi-modal sensing payloads facilitate image registration, as there is a

Further author information: (Send correspondence to Andrew M. Duncan)
Andrew M. Duncan: E-mail: duncanam@ornl.gov

central, integrated GPS-INS (Global Positioning System, Inertial Navigation System) unit to which all sensors reference flight data. Examples of airborne multi-modal sensing payloads presently include the LiCHy Airborne Observation System, containing LIDAR, a charged-coupled device, and hyperspectral,[25] the Carnegie Airborne Observatory's hyperspectral and LIDAR system,[26] and NASA Goddard Space Flight Center's G-LiHT system, containing LIDAR, hyperspectral and thermal imaging instruments.[24] While piloted airborne payloads can offer more flexibility than satellite platforms, in terms of spatial and temporal resolution, airborne platforms can be expensive to mobilize and require extensive planning in the lead up to a campaign.

Use of small unmanned aerial systems (UAS) as remote sensing platforms has become more popular as hardware becomes more efficient and integration and operational costs are reduced. Previously, UAS lacked the ability to carry more than one sensor at a time, so if a survey required more than one sensor modality, each was flown individually.[27] Fortunately, recent advancements in sensor technology have resulted in significant reductions in size, weight, and power (SWaP) specifications that now permit multi-sensor payload integrations. Since UAS can be operated at low altitudes not accessible to larger or piloted aircraft,[28] and can be rapidly mobilized, UAS can now provide high spatial and temporal resolutions that outperform that of higher altitude aircraft and satellite platforms.

Since UAS-compatible sensors are still relatively new to the market, fewer examples of multi-modal UAS payloads exist. One example is the MX-1 UAS payload operated by the Rochester Institute of Technology (RIT). RIT has successfully integrated four sensors; hyperspectral, LIDAR, LWIR (long-wave infrared/thermal), and RGB (visible). To our knowledge, the MX-1 payload integrates the most comprehensive UAS sensing payload.

In this paper, we present a new multi-modal UAS payload which approaches the sensing capabilities that the remote sensing community has come to expect from a larger aircraft with greater carrying capacity. Our system, which we call ARTEMIS (Advanced Rotorcraft Telemetry-Equipped Multi-Modal Imaging System), integrates five sensing modalities; RGB, multispectral, hyperspectral, thermal, and LIDAR, on one platform.

2. DESIGN AND INSTRUMENTATION

2.1 Strelka Aircraft

The Oak Ridge National Laboratory's Strelka unmanned aircraft (Figure 1a) was designed by the ORNL Unmanned Vehicle Development Laboratory (UVDL) as a SWaP-optimized unmanned quadcopter designed to carry modular scientific payloads (Figure 1b). The aircraft is an electric quadcopter designed for maximum efficiency and is powered by a 22 amp hour 12S battery turning 28-inch carbon fiber propellers for a maximum flight time of 45 minutes with payloads of up to 12 pounds. The aircraft features include a custom-designed avionics board which integrates a Pixhawk 2.1 Cube flight controller with a power distribution circuit board which includes redundant power supplies and power monitoring circuits on a single printed circuit board weighing less than 300 grams. The avionics board eliminates the need for heavy wiring harnesses, thus increasing flight time and payload capabilities. The avionics board also includes multiple UART (universal asynchronous receiver transmitter) interfaces which are used to provide telemetry information to the payload permitting front-end data processing. The Strelka utilizes the open-sourced Arducopter firmware for basic flight control.

2.2 Velodyne LiDAR

The Velodyne Puck LITE (Figure 2) is a high-resolution LIDAR sensor which was chosen for use on the UAS platform due to its lightweight (590 g) design. The Puck LITE uses a 903 nm Class 1 laser that captures 300,000 points s^{-1} and 600,000 points s^{-1} in single and dual return mode respectively. The sensor has 16 laser/detector pairs rotating at a rate of 5-20 Hz and an operating range of approximately 100 m. It captures a 360° horizontal FOV at an angular resolution of 0.1° - 0.4° while the vertical FOV is 30° with an angular resolution of 2.0°. Each data packet includes time of flight distance measurement, calibrated reflectivity measurement, rotation angles, and synchronized time stamps.[29]

(a) Strelka platform (b) Platform with multi-modal payload

Figure 1: Fully assembled platform and payload integration. Tape measure of 12 inches is shown for scale.

2.3 MicaSense Multispectral Imager

The MicaSense RedEdge-M multispectral sensor (Figure 2) was designed specifically for use onboard a UAS platform. With its compact and lightweight design (9.4 x 6.3 x 4.6 cm; 150 g) the sensor can be adapted to both fixed wing and multi-rotor systems. The sensor has a spectral range of 400 900 nm with a 47.2° field of view (FOV). It has five spectral bands, blue, green, red, red edge (RE), and near-infrared (NIR). Spectral bands have a ground sampling distance (GSD) of 8.2 cm at 120 m above ground level (Table 1). A global shutter is aligned with all bands with a 12-bit radiometric resolution at an image capture rate of 1 Hz. Coupled to the multispectral sensor is a downwelling light sensor (DLS). The DLS is used in association with a calibrated reflectance panel to improve reflectance calibrations along with the radiometric quality of the data. The DLS is mounted on top of the UAS and captures data throughout the flight on changes in light conditions.[30]

Table 1: MicaSense RedEdge-M sensor characteristics

Spectral Band	Wavelength (nm)	GSD (cm)
Blue	465 - 485	
Green	550 - 570	
Red	663 - 673	8.2
Red Edge	712 - 722	
Near-Infrared	820 - 860	

2.4 Resonon Hyperspectral Imager

The Resonon Pika L (Figure 2) is a high spectral and spatial resolution compact hyperspectral sensor (10.0 x 12.5 x 5.3 cm; 600 g). The Pika L operates between the 400-1000 nm spectral region with a spectral resolution of 2.1 nm which allows for 281 spectral bands at 12-bit radiometric resolution. The sensor accepts a 17 mm (f/2.4; 17.6° FOV) visible-NIR objective lens which produces up to 5.86 µm pixel size and a max capture rate of 249 Hz.[31]

2.5 FLIR Thermal Imager

The FLIR Duo Pro R (Figure 2) is a dual-sensor thermal and infrared light imager. The small UAS sensor (8.5 x 8.1 x 6.9 cm; 325 g) measures long wave infrared (LWIR) over a spectral range of 7.5 - 13.5 µm using an uncooled VOx microbolometer with a thermal sensitivity of $<$ 50 mK at a 30 Hz frame rate. It uses a 25 mm optical lens which provides a thermal sensor resolution of 640 x 512 pixels and a 25° x 20° FOV. The dedicated RGB (red green blue) visible sensor has a resolution of 4000 x 3000 pixels with a FOV of 56° x 45°. Integrated within the thermal imaging system are sensors for temperature, humidity, and altitude, which deliver radiometrically calibrated data (accuracy +/- 5° C between the range of -25° - 135° C). Other sensor features

include MSX image enhancement (combines both visible and thermal spectrums into one image), infrared-only, and visible-only imaging.[32]

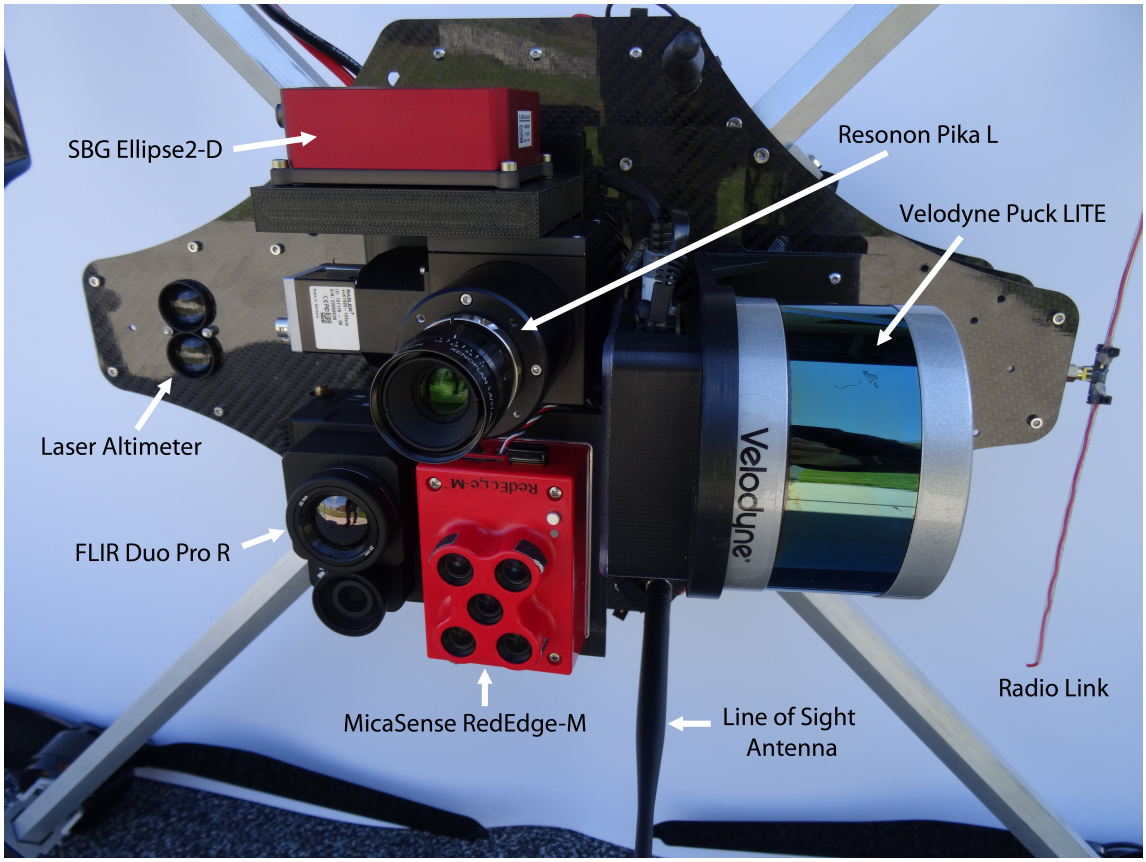

Figure 2: Suite of ARTEMIS sensors which include the MicaSense RedEdge-M (multispectral), FLIR Duo Pro R (thermal and RGB), Resonon Pika L (hyperspectral), and Velodyne Puck LITE (LIDAR) sensors. The payload also includes a downward facing laser altimeter, and SBG Ellipse2-D GPS/GNSS/IMU.

3. POSITIONING SYSTEMS

3.1 Navigation

The aircraft uses two Global Navigation Satellite Systems (GNSS), the uBlox M8N Micro GPS and the Here GNSS GPS, which send positioning data to the flight controller. Both systems contain U-Blox NEO-M8N modules which can allow for concurrent reception of up to three GNSS signals (GPS, Galileo, GLONASS, BeiDou) and 167 dBm navigation sensitivity. The uBlox has an update rate of 10 Hz and has a small form factor (25 x 25 x 4 mm, 20.6 g).[33] The Here GNSS GPS supports all satellite augmentation systems, advanced jamming and spoofing detection, as well as security and integrity protection.[34]

Also included on the aircraft is a Lightware SF11/C laser altimeter. This light-weight downward facing laser altimeter has a long range of 120 m and was specifically designed for UAS platforms. It provides fast and accurate above ground altitude information that can allow the platform to follow terrain.[35]

3.2 Sensor Geolocation

ARTEMIS imaging sensors (LIDAR, multispectral, hyperspectral, thermal, and RGB) all receive positioning data from the SBG Ellipse2-D INS/GNSS (87 x 67 x 31.5 mm, 180 g), shown in Figure 3. The Ellipse2-D's inertial measurement unit (IMU) has 3 axis gyroscopes, 3 axis accelerometers, 3 axis magnetometers, and temperature

sensors. It is also integrated with a dual-antenna survey grade RTK GNSS for a heading accuracy of 0.2° and a roll/pitch accuracy of 0.1°/0.05°. The system has an output rate of 200 Hz and 1000 Hz for GNSS and IMU respectively.[36]

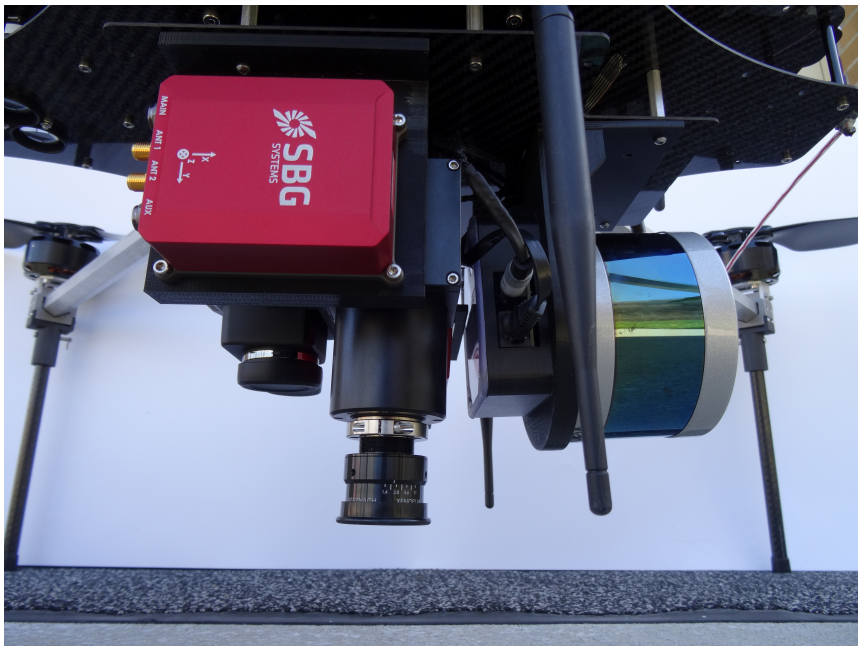

Figure 3: Side view of the ARTEMIS payload. Currently visible sensors are the FLIR Duo Pro R, Resonon Pika L, and Velodyne Puck LITE as well as line of sight antennas and SBG GNSS/IMS system.

4. SENSOR INTEGRATION

The ARTEMIS payload connects all the sensors to an NVidia Jetson TX2 compute module to enable all data products to be collected into a single storage device for easy retrieval following the flight (Figure 4).

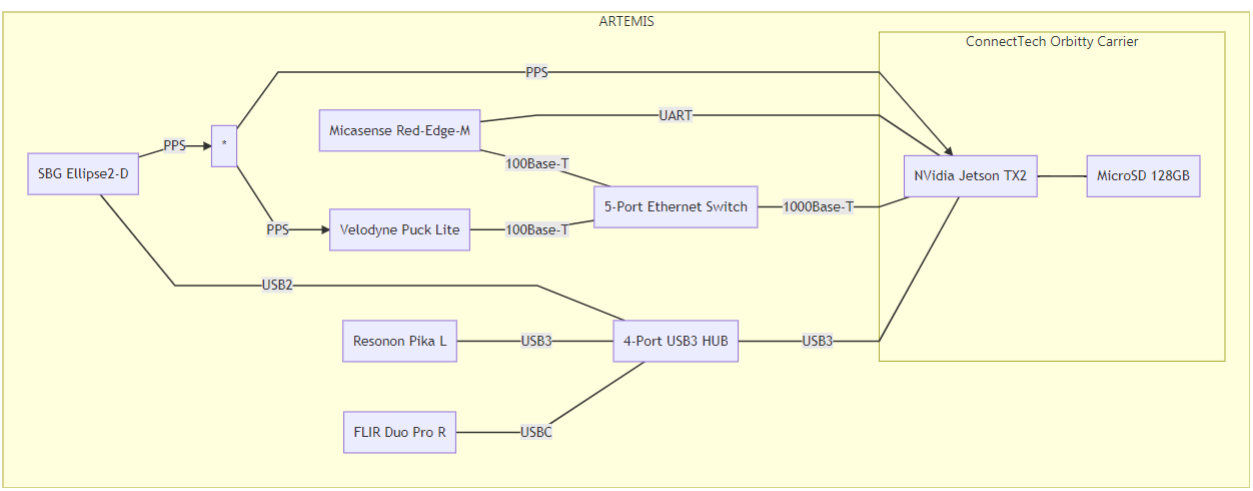

Figure 4: Data connections on the ARTEMIS payload. PPS stands for Pulse-per-Second. PPS is sourced by the SBG GNSS and distributed to the LIDAR and the TX2 for time synchronization.

4.1 High Resolution Position and Attitude

The SBG[36] produces location telemetry at 200Hz and inertial telemetry at 1000Hz which are interpreted by a program implemented with SBG System's Unix SDK[37] and written into an SQL (Structured Query Language) database on the TX2 that can be queried asynchronously during the flight for geotagging of the data products in real-time. The database schema is defined as follows (Listing 1):

```
KEYS = {
    'time_unix_usec':{ 'type':'integer', 'modifier':'PRIMARY KEY', 'source':'SYSTEM_TIME', 'scale':1 },
    'time_boot_ms':{ 'type':'integer', 'modifier':'NOT NULL', 'source':'SYSTEM_TIME', 'scale':1 },
    'lat':{ 'type':'real', 'modifier':'NOT NULL', 'source':'GLOBAL_POSITION_INT', 'scale':1e7 },
    'lon':{ 'type':'real', 'modifier':'NOT NULL', 'source':'GLOBAL_POSITION_INT', 'scale':1e7 },
    'alt':{ 'type':'real', 'modifier':'NOT NULL', 'source':'GLOBAL_POSITION_INT', 'scale':1e3 },
    'relative_alt':{ 'type':'real', 'modifier':'NOT NULL', 'source':'GLOBAL_POSITION_INT', 'scale':1e3 },
    'hdg':{ 'type':'real', 'modifier':'NOT NULL', 'source':'GLOBAL_POSITION_INT', 'scale':1e2 },
    'roll':{ 'type':'real', 'modifier':'NOT NULL', 'source':'ATTITUDE', 'scale':1.0 },
    'pitch':{ 'type':'real', 'modifier':'NOT NULL', 'source':'ATTITUDE', 'scale':1.0 },
    'yaw':{ 'type':'real', 'modifier':'NOT NULL', 'source':'ATTITUDE', 'scale':1.0 },
    'rollspeed':{ 'type':'real', 'modifier':'NOT NULL', 'source':'ATTITUDE', 'scale':1.0 },
    'pitchspeed':{ 'type':'real', 'modifier':'NOT NULL', 'source':'ATTITUDE', 'scale':1.0 },
    'yawspeed':{ 'type':'real', 'modifier':'NOT NULL', 'source':'ATTITUDE', 'scale':1.0 },
    'groundspeed':{ 'type':'real', 'modifier':'NOT NULL', 'source':'VFR_HUD', 'scale':1.0 },
}
```

Listing 1: (Python) Database schema for telemetry database to correlate time with position and attitude.

A new entry in the database is produced upon any change to any of the keys. The **time_unix_usec** is the monotonically increasing primary key. The **source** field references the MAVLink message from where the field key is obtained as the telemetry extraction code is also used to produce database files from flight controller telemetry. We found that producing multiple database files was useful when post-processing because time keeping between the flight controller and the companion computer had variations. The **scale** field represents the scaling that is applied to the value in the MAVLink message.

4.2 LIDAR Telemetry Processing

In order to operate correctly, the Velodyne Puck LIDAR requires NMEA location information to be sent over its network connection to TCP/IP port 10110. We accomplished this in a variety of ways as we developed the payload.

- Using **gpsd** to configure a GPS device over USB/UART
- Interpreting MAVLink telemetry and synthesizing an NMEA stream from it
- Interpreting the SBG position telemetry and synthesizing NMEA stream from it

We found that the Velodyne LIDAR did not operate when sent anything except the **$GPRMC** sentence, so we filtered everything else out before passing the stream through to the LIDAR port. We did this in a **systemd** service that called a **bash** command to do the work (Listing 2):

```
/usr/bin/gpspipe -r | /bin/grep ^\$GPRMC | /bin/nc 192.168.1.201 10110
```

Listing 2: (Bash) Command line for providing LIDAR with position

The LIDAR also needs a PPS (Pulse-per-Second) signal to correctly calculate the laser returns. This was done by wiring the PPS output of the GPS/SBG to both the LIDAR PPS input and a TX2 GPIO (General Purpose Input Output) input. The LIDAR broadcasts its raster data on UDP (User Datagram Protocol) port

2368 and its position information on port 8308. Software exists for processing these raw packets. An efficient method to capture this data is to use **tcpdump** to generate a **.pcap** file. It is important to ensure that captured data is written to disk periodically, and it is best to limit the size of the capture file; **tcpdump** can do this (Listing 3). This is the command we used (called from a **systemd** service):

```
/usr/sbin/tcpdump -i eth0 -Z nvidia -s 0 -C 100 -W 99 -w /var/log/mavnet/velodyne \
   host 192.168.1.201 and \( port 2368 or port 8308 \)
```

Listing 3: (Bash) Command line for capturing size-limited LIDAR files

4.3 Imagery

4.3.1 Micasense

The Micasense produces Tagged Image File Format files (**.tiff**) that are stored on its internal SD card. They provide an API[38] (application programming interface) and Python[39] example code to access the pictures stored on the camera. The TX2 access the camera using the HTTP API over its wired ethernet connection at the default address of 192.168.1.83.

The Micasense camera serial port is connected to a Pixhawk flight controller telemetry port and so responds interprets the MAVLink messages **DIGICAM_CONFIGURE** and **DIGICAM_CONTROL**. It emits **CAMERA_STATUS** and **CAMERA_FEEDBACK**. These are relayed by the flight controller to the TX2 over its own telemetry link port, and stored in Mission Planner[40]-compatible **.tlog** files.

A Mission Planner-compatible **.tlog** file is simply a binary file containing packed MAVLink messages interleaved with a 64-bit timestamp representing the number of microseconds since Jan 1, 1970 (big-endian byte ordered).

4.3.2 Resonon

The Resonon Pika L provides an C++ API[41] to setup and control the camera. The API is distributed via **.dll** files compiled for the Windows OS. ARTEMIS uses a Linux OS on the TX2, so we could not use this API directly. Fortunately, the Pika L uses a Basler ACE U[42] camera connected via USB3.0, and the Basler pylon[43] software can be used to interface to the camera and collect images. The USB port was connected to a 4-port USB3 HUB to allow the TX2 to access it. We used **pypylon**[44] to perform captures that were synchronized with MAVLink **DIGICAM_CONTROL** messages interpreted by the TX2.

4.3.3 FLIR

The FLIR Duo Pro R can be configured to produce **.jpg** files that contain both RGB and thermal on different layers. An Android or iOS phone is used to setup the camera over a Bluetooth wireless link.[32] The camera contains its own GPS and IMU to geotag the images that it produces. All images are stored on one of two microSD cards that are fitted into the camera. We observed that only one microSD card is used for image data storage.

The pulse width modulation (PWM) input is used to trigger the camera to take a picture and this signal is wired to the flight controller. This allows missions to control when the picture is taken. Although the Duo Pro R can be configured to receive MavLink messages via one of its other PWM inputs, and include this information into the metadata fields of the images it produces, we did not take advantage of this capability to date. We did observe that the EXIF (Exchangeable Image File) GPS information was not reliably added to the **.jpg** files produced by the camera.

The Duo Pro R USB port is connected to the TX2 via USB-C to the USB3 hub using a suitably terminated cable. When connected in this way, the microSD cards are seen as mass storage devices and can be accessed by the TX2.

4.3.4 Geotagging

In order to be used by photogrammetry software, every data product produced by the ARTEMIS payload must be correctly identified with is location. In addition, the offset from the appropriate GPS antenna position on the platform and the center of the camera must also be applied. Some of the imagery files collected contain position information while others do not, so we tag all files produced in a consistent manner.

During the flight, a process on the TX2 interfaces with the various sensors and copies the data products to the internal filesystem on the TX2. The references to those files are added by this process to an SQL database on the TX2 that can be queried asynchronously during the flight for geotagging (Listing 4). The database schema is as follows:

```
KEYS = {
    'External_Cmd_ID': {'type': 'integer', 'modifier': 'NOT NULL'},
    'Camera_IP': {'type': 'text', 'modifier': 'NOT NULL'},
    'File_Path': {'type': 'text', 'modifier': 'NOT NULL'},
    'TimeStamp_Before_actTakePicture': {'type': 'integer', 'modifier': 'NOT NULL'},
    'TimeStamp_After_actTakePicture': {'type': 'integer', 'modifier': 'NOT NULL'},
    'TimeStamp_URLRetrieve': {'type': 'integer', 'modifier': 'NOT NULL'},
    'TimeStamp_EXIFTools_Complete': {'type': 'integer', 'modifier': ''},
}
```

Listing 4: (Python) Database schema for image database to update EXIF information with.

A new entry in the database is produced when a new file is added. The **File_Path** is the location of the file in the TX2 filesystem. The **TimeStamp_EXIFTools_Complete** field is a boolean that indicates that geotagging is complete on this file. The remaining fields are used for support of an imaging system that is not part of the ARTEMIS payload as well as track latency between command steps for diagnostics.

A separate process on the TX2 queries the photo database and performs work to update the EXIF information in the unprocessed files. This process runs a Python script that continuously performs the following steps:

1. query photo.db for records with 0 Timestamp_EXIFTOOLS_Complete
2. iterate over unprocessed photos
   (a) extract external_cmd_id, timestamp, file_locations
   (b) use artemis/location.py to interpolate position & heading based on timestamp
   (c) call exiftool cmd line to overwrite the info
3. wait x seconds

In this way, the photo database is used to sequence the work needed so that multiple processes do not access the same files without resorting to complex locking and signalling methods.

4.4 Companion Computer Processing

In addition to the processing necessary to update the telemetry database and the processes that copy the imagery and output files from the sensors, the TX2 also ensures that the external micro SD card is kept updated with the data products during the flight. As it does so, it keeps track of the file system health and ensures that data product files copied successfully to the external micro SD card are removed from the internal file system.

Finally, the use of the TX2 in the ARTEMIS sensor package was primarily driven by the desire to perform additional edge processing so as to reduce the time needed for follow-on photogrammetry and processing to produce orthomosaic projections.

5. COMMUNICATION SYSTEM AND FLIGHT PLANNING

5.1 Communication System

The Strelka aircraft leverages the Multimodal Autonomous Vehicle Network (MAVNet) next-generation communication system designed for Beyond-Visual-Line-Of-Sight (BVLOS) operations. The MAVNet system combines an on-board co-processor with a 2.4Ghz line-of-sight telemetry radio, Cellular LTE modem and an Iridium Short Burst Data modem to provide robust global communications and on-board data processing capabilities. These radios provide reliable internet access to the aircraft which enables aircraft command and control through a web-based graphical user interface. A patent-pending monotonic logic generator provides message de-duplication to accommodate the differing latencies associated with each radio. MAVNet provides multiple-pilot operation and extremely long-range communication capabilities and is also used to generate custom messages for controlling the various sensors on the aircraft.

5.2 Flight Planning

MAVNet enables shared flight planning capabilities among operators and data analysts as well as permits real-time monitoring of video and telemetry information while the aircraft is in operation, regardless of the physical distance between the operator, aircraft and researcher. The graphical user interface (GUI) is hosted on a web server which enables authorized users to access the ground control station via any standard web browser. With this new architecture, the researcher is able to plan a flight utilizing the GUI and share that flight plan with the operator prior to the flight. The remote pilot in command may then review the flight plan for safety and compliance with the operating regulations prior to conducting the flight. While the aircraft is in operation, the researcher may then monitor the real-time flight telemetry and video to provide feedback to the operator that may enhance data quality.

6. CONCLUSION

Oak Ridge National Laboratory's Advanced Rotorcraft Telemetry-Equipped Multi-Modal Imaging System (ARTEMIS) permits data collection from five different remote sensing modalities; multispectral, hyperspectral, thermal, RGB and LIDAR. These sensors use one common GNSS and inertial navigation system which allows for imagery and data products from all sensors to be accurately and precisely geolocated and co-registered. What makes this platform unique is our MAVNet communication system which will allow for BVLOS operations. MAVNet utilizes line-of-sight telemetry radio, cellular LTE, and Iridium Short Burst Data, which prevent lost link situations between the ground control station and platform as well as platform control over all three. MAVNet also serves as our flight planning software with an intuitive GUI which can be accessed via web server and allows for multiple users to review, change, and execute flight plans.

The motivation for ARTEMIS is to collect accurately co-registered data from multiple modalities in a single flight with high spatial and temporal resolution. Capturing data with all modalities at once minimizes operational and data processing time as well as cost. Commercial sensors were chosen due to their lower cost and availability in comparison to other multi-modal airborne systems which use custom sensors.[26] The ARTEMIS payload is a modular package meaning that sensors can easily be swapped. The payload package can be easily be integrated into other unmanned platforms such as fixed wing and VTOL (vertical take-off and landing).

We see ARTEMIS's capabilities being used in a variety of research applications including, forestry, agriculture, environmental monitoring, mapping, as well as search and rescue. While each of these remote sensing modalities can provide suitable information on their own, by collecting all of them at once can lead to more useful and complete data products.

ACKNOWLEDGMENTS

The authors wish to acknowledge valuable contributions made by Bradley Rueter, Andrew Harter, Brad Stinson, Alexandra Hackett, and Thad Thompson.

This manuscript has been authored by UT-Battelle, LLC, under Contract No. DE-AC05-00OR22725 with the U.S. Department of Energy. The United States Government retains and the publisher, by accepting the article

for publication, acknowledges that the United States Government retains a non-exclusive, paid-up, irrevocable, world-wide license to publish or reproduce the published form of this manuscript, or allow others to do so, for United States Government purposes.

REFERENCES

[1] Jackson, T. J., Chen, D., Cosh, M., Li, F., Anderson, M., Walthall, C., Doriaswamy, P., and Hunt, E. R., "Vegetation water content mapping using Landsat data derived normalized difference water index for corn and soybeans," *Remote Sensing of Environment* **92**(4), 475–482 (2004).

[2] Li, P., Jiang, L., and Feng, Z., "Cross-comparison of vegetation indices derived from landsat-7 enhanced thematic mapper plus (ETM+) and landsat-8 operational land imager (OLI) sensors," *Remote Sensing* **6**(1), 310–329 (2013).

[3] Costa, A. P., De Souza Filho, C. R., Azevedo, F., and Brodie, C., "Targeting key alteration minerals in epithermal deposits in Patagonia, Argentina, using ASTER imagery and principal component analysis," *International Journal of Remote Sensing* **24**(21), 4233–4240 (2003).

[4] van der Meer, F. D., van der Werff, H. M., van Ruitenbeek, F. J., Hecker, C. A., Bakker, W. H., Noomen, M. F., van der Meijde, M., Carranza, E. J. M., de Smeth, J. B., and Woldai, T., "Multi- and hyperspectral geologic remote sensing: A review," *International Journal of Applied Earth Observation and Geoinformation* **14**(1), 112–128 (2012).

[5] Xian, G. and Crane, M., "Assessments of urban growth in the Tampa Bay watershed using remote sensing data," *Remote Sensing of Environment* **97**(2), 203–215 (2005).

[6] Cooner, A. J., Shao, Y., and Campbell, J. B., "Detection of urban damage using remote sensing and machine learning algorithms: Revisiting the 2010 Haiti earthquake," *Remote Sensing* **8**(10) (2016).

[7] Vincent, R. K., Qin, X., McKay, R. M. L., Miner, J., Czajkowski, K., Savino, J., and Bridgeman, T., "Phycocyanin detection from LANDSAT TM data for mapping cyanobacterial blooms in Lake Erie," *Remote Sensing of Environment* **89**(3), 381–392 (2004).

[8] Barrett, D. and Frazier, A., "Automated Method for Monitoring Water Quality Using Landsat Imagery," *Water* **8**(6), 257 (2016).

[9] Chang, J., Clay, D. E., Dalsted, K., Clay, S., and O'Neill, M., "Corn (L.) Yield Prediction Using Multispectral and Multidate Reflectance," *Agronomy Journal* **95**(6), 1447 (2003).

[10] Wojtowicz, M., Wojtowics, A., and Piekarczyk, J., "Application of remote sensing methods in Agriculture," *Communication in Biometry and Crop Science* **11**(1), 31–50 (2016).

[11] Urqueta, H., Jódar, J., Herrera, C., Wilke, H.-G., Medina, A., Urrutia, J., Custodio, E., and Rodríguez, J., "Land surface temperature as an indicator of the unsaturated zone thickness: A remote sensing approach in the Atacama Desert," *Science of The Total Environment* **612**, 1234–1248 (jan 2018).

[12] Blackett, M., "Early analysis of landsat-8 thermal infrared sensor imagery of volcanic activity," *Remote Sensing* **6**(3), 2282–2295 (2014).

[13] Hoffmann, H., Nieto, H., Jensen, R., Guzinski, R., Zarco-Tejada, P. J., and Friborg, T., "Estimating evapotranspiration with thermal UAV data and two source energy balance models," *Hydrology and Earth System Sciences Discussions* **12**(8), 7469–7502 (2015).

[14] Loheide, S. P. and Gorelick, S. M., "Quantifying stream-aquifer interactions through the analysis of remotely sensed thermographic profiles and in situ temperature histories," *Environmental Science and Technology* **40**(10), 3336–3341 (2006).

[15] Tamborski, J. J., Rogers, A. D., Bokuniewicz, H. J., Cochran, J. K., and Young, C. R., "Identification and quantification of diffuse fresh submarine groundwater discharge via airborne thermal infrared remote sensing," *Remote Sensing of Environment* **171**, 202–217 (dec 2015).

[16] Asner, G. P., Townsend, P. a., Martin, R. E., and Chadwick, K. D., "Forest Biophysical and Biochemical Properties from Hyperspectral and LiDAR Remote Sensing," in [*Land Resources Monitoring, Modeling, and Mapping with Remote Sensing*], Thenkabail, P., ed., ch. Forest bio, 429–448, CRC Press, Taylor & Francis Group (2015).

[17] Matikainen, L., Lehtomäki, M., Ahokas, E., Hyyppä, J., Karjalainen, M., Jaakkola, A., Kukko, A., and Heinonen, T., "Remote sensing methods for power line corridor surveys," *ISPRS Journal of Photogrammetry and Remote Sensing* **119**, 10–31 (2016).

[18] Dalponte, M., Bruzzone, L., and Gianelle, D., "Fusion of hyperspectral and LIDAR remote sensing data for classification of complex forest areas," *IEEE Transactions on Geoscience and Remote Sensing* **46**(5), 1416–1427 (2008).

[19] Swatantran, A., Dubayah, R., Roberts, D., Hofton, M., and Blair, J. B., "Mapping biomass and stress in the Sierra Nevada using lidar and hyperspectral data fusion," *Remote Sensing of Environment* **115**(11), 2917–2930 (2011).

[20] Sankey, T. T., McVay, J., Swetnam, T. L., McClaran, M. P., Heilman, P., and Nichols, M., "UAV hyperspectral and lidar data and their fusion for arid and semi-arid land vegetation monitoring," *Remote Sensing in Ecology and Conservation* **4**(1), 20–33 (2018).

[21] Irwin, K., Beaulne, D., Braun, A., and Fotopoulos, G., "Fusion of SAR, optical imagery and airborne LiDAR for surface water detection," *Remote Sensing* **9**(9), 1–18 (2017).

[22] Olsoy, P. J., Mitchell, J., Glenn, N. F., and Flores, A. N., "Assessing a multi-platform data fusion technique in capturing spatiotemporal dynamics of heterogeneous dryland ecosystems in topographically complex terrain," *Remote Sensing* **9**(10) (2017).

[23] Alonzo, M., Bookhagen, B., and Roberts, D. A., "Urban tree species mapping using hyperspectral and lidar data fusion," *Remote Sensing of Environment* **148**(JANUARY), 70–83 (2014).

[24] Cook, B. D., Corp, L. A., Nelson, R. F., Middleton, E. M., Morton, D. C., McCorkel, J. T., Masek, J. G., Ranson, K. J., Ly, V., and Montesano, P. M., "NASA goddard's LiDAR, hyperspectral and thermal (G-LiHT) airborne imager," *Remote Sensing* **5**(8), 4045–4066 (2013).

[25] Pang, Y., Li, Z., Ju, H., Lu, H., Jia, W., Si, L., Guo, Y., Liu, Q., Li, S., Liu, L., Xie, B., Tan, B., and Dian, Y., "LiCHy: The CAF's LiDAR, CCD and hyperspectral integrated airborne observation system," *Remote Sensing* **8**(5), 1–16 (2016).

[26] Asner, G. P., "Carnegie Airborne Observatory: in-flight fusion of hyperspectral imaging and waveform light detection and ranging for three-dimensional studies of ecosystems," *Journal of Applied Remote Sensing* **1**(1), 013536 (2007).

[27] Turner, D., Lucieer, A., Malenovský, Z., King, D. H., and Robinson, S. A., "Spatial co-registration of ultra-high resolution visible, multispectral and thermal images acquired with a micro-UAV over antarctic moss beds," *Remote Sensing* **6**(5), 4003–4024 (2014).

[28] Zeng, C., King, D. J., Richardson, M., and Shan, B., "Fusion of multispectral imagery and spectrometer data in UAV remote sensing," *Remote Sensing* **9**(7) (2017).

[29] Velodyne, "VLP-16 (Puck LITE)," (2018). Available=https://velodynelidar.com/vlp-16-lite.html.

[30] MicaSense, "RedEdge-M," (2018). Available=https://www.micasense.com/rededge-m/.

[31] Resonon, "Pika L," (2018). Available=https://resonon.com/pika-l-camera.

[32] FLIR, *FLIR Duo Pro R User Guide, Version 1.0* (2017). Available=https://www.flir.com/globalassets/imported-assets/document/duo-pro-r-user-guide-v1.0.pdf.

[33] Holybro, "Micro M8N GPS," (2009). Available=http://www.holybro.com/product/22.

[34] Here, "Here GNSS," (2017). Available=http://www.hex.aero/wp-content/uploads/2017/08/HERE-USER-GUIDE-ENG.pdf.

[35] Lightware, "SF11/C (120 m) LightWare Optoelectronics." Available=https://lightware.co.za/collections/lidar-rangefinders/products/sf11-c-120-m.

[36] SBG, "Ellipse 2-D." Available=https://www.sbg-systems.com/products/ellipse-2-series/.

[37] SBG, "Ellipse Series and Ellipse Micro Support Information." Available=https://www.sbg-systems.com/ellipse-ellipse-micro-support/.

[38] MicaSense, "Micasense RedEdge API," (2019). Available=http://micasense.github.io/rededge-api/.

[39] van Rossum, G. and (eds), F. L. D., *Python Reference Manual*. PythonLabs, Virginia, USA (2001). Available=http://www.python.org.

[40] Oborne, M., "Mission Planner," (2019). Available=http://ardupilot.org/planner/.

[41] Resonon, *Resonon C++ API for controlling Resonon hyperspectral imagers* (2019). Available=http://docs.resonon.com/API/html/index.html.

[42] Basler AG, "Basler acA1920-155uc USB 3.0 camera with the Sony IMX174 CMOS," (2019). Available=https://www.baslerweb.com/en/products/cameras/area-scan-cameras/ace/aca1920-155uc/.

[43] Basler AG, "Basler Pylon Software for Embedded Vision Applications," (2019). Available=https://www.baslerweb.com/en/products/software/pylon-linux-arm/.

[44] Basler AG, "Python wrapper for Basler pylng Camera Software Suite," (2019). Available=https://github.com/basler/pypylon.